Doped Nickel Oxide Carrier-Selective Contact for Silicon Solar Cells: A Computational Study

Journal:	*Journal of Photovoltaics*
Manuscript ID	JPV-2021-05-0186-R
Manuscript Type:	Regular
Date Submitted by the Author:	11-May-2021
Complete List of Authors:	Hossain, Md Anower; University of New South Wales - Kensington Campus, School of Photovoltaic and Renewable Energy Engineering Zhang, Tian; University of New South Wales - Kensington Campus, School of Photovoltaic and Renewable Energy Engineering Zakaria, Yahya; Hamad Bin Khalifa University, Qatar Environment and Energy Research Institute Lambert, Daniel; University of New South Wales - Kensington Campus, School of Photovoltaic and Renewable Energy Engineering Burr, Patrick; University of New South Wales, School of Mechanical and Manufacturing Engineering Rashkeev, Sergey; University of Maryland at College Park, Materials Science and Engineeingg Abdallah, Amir ; Hamad Bin Khalifa University, Qatar Environment and Energy Research Institute Hoex, Bram; University of New South Wales - Kensington Campus, School of Photovoltaic & Renewable Energy Engineering
Keywords:	Density functional theory, Silicon photovoltaics, Hole-selective passivation contact, Transition metal oxides, Nickel oxide, Dopants

Doped Nickel Oxide Carrier-Selective Contact for Silicon Solar Cells: A Computational Study

Md. Anower Hossain, Tian Zhang, Yahya Zakaria, Daniel Lambert, Patrick A Burr, Sergey N Rashkeev, Amir Abdallah, and Bram Hoex

***Abstract*—Transition metal oxides such as MoO_3, WO_3, V_2O_5 and NiO have shown potential as hole-selective passivating contact for silicon (Si) solar cells. Among them, NiO is a notoriously poor hole-conducting semiconductor. Doping of metal oxides with multivalent metal cations is an effective method to modify their electronic properties because dopant-induced favorable defect states play crucial for charge carrier transport in device applications. We use first-principles density functional theory (DFT) to identify suitable metal cations that favorably affect the hole-conducting properties of NiO. We identify Al, Mg and Zn as suitable dopants for NiO, improving ohmic contact properties with c-Si. Subsequently, Al-doped NiO (Al_xNi_yO) films were synthesized onto c-Si using an atomic layer deposition supercycle approach. The Al_xNi_yO films showed a contact resistivity of 41.6 - 113 mΩ cm^2 with c-Si after annealing at 200-300 °C, in contrast to undoped NiO where no ohmic contact could be formed. This in-depth computational study followed by the experimental synthesis of Al_xNi_yO films remove a critical barrier for the future applications of NiO based carrier-selective passivating contacts for c-Si and other types of solar cells, as well as providing a path for the optimization of other functional materials.**

***Index Terms*—Density functional theory (DFT), Nickel oxide (NiO), p-type conductivity, Passivation contact, Si photovoltaics, Density of states (DOS)**

I. INTRODUCTION

Transition metal oxides (TMOs) are low-cost, earth-abundant semiconducting materials, which are important for a wide range of applications, such as water splitting,[1] gas sensing,[2] solar cells,[3-7] electrocatalysis,[8] energy storage,[9] and electrochromic displays.[10] TMOs may contain inherent, intrinsic vacancies and interstitial defects and extrinsic impurity-related defects, which significantly affect their electronic and optical properties. Therefore, extensive efforts have been taken to study defects in the TMOs to identify favorable combinations of defects and impurities that can significantly improve the final device performance. TMOs with a large work function and shallow defect states close to their conduction band (CB) or valence band (VB) are needed for an efficient collection of photogenerated charge carriers from crystalline silicon (c-Si). For NiO, shallow defect states at the VB are required as it is an appealing hole-collector due to its small band offset with the c-Si VB.[11]

Stoichiometric NiO is a Mott-Hubbard insulator[12] with an extremely low electrical conductivity ($<10^{-13}$ Ω^{-1} cm^{-1}) at room temperature.[13] However, a typical NiO film is non-stoichiometric and contains nickel vacancies (V_{Ni}), which are charge compensated by holes localized at Ni sites (Ni^{3+}) when the film is grown in excess oxygen conditions. These intrinsic defects make NiO a *p*-type semiconducting material with a hole mobility of 1.15×10^{-3} m^2 V^{-1}s^{-1}.[14] The reasonable hole conductivity combined with a relatively large bandgap of 3.4 – 4 eV,[3] makes NiO a favorable hole-transporting material for perovskite,[6, 15] quantum-dot,[7] and silicon solar cells.[4] However, both a poor material conductivity plus intricate defect chemistry at the NiO/c-Si interface limit the power conversion efficiency of NiO-based silicon solar cells.

It is well known that the incorporation of extrinsic defects can change the electronic properties of semiconductors. It has been shown that substitutional Li, Na, and K on Ni-sites significantly increase the hole concentration in NiO as all of these atoms are all monovalent in contrast to Ni, which is typically divalent. In the case of Li, which has a similar ionic radius (0.76 Å) compared to Ni^{2+} (0.69 Å), the increased concentration of trivalent Ni thereby further enhances the NiO *p*-type conductivity (up to 11.2 S.cm^{-1}), work function (up to 5.04 eV) as well as the hole concentrations (up to 6.13×10^{21}).[16] However, Li-doped NiO is shown to have a low charge carrier mobility of 5×10^{-3} m^2 V^{-1} s^{-1},[16] and its integration in an *n*-type c-Si heterojunction solar cell only resulted in a modest champion efficiency of 6.3%.[17] Incorporation of Na and K improves the *p*-type conductivity of NiO film with resistivity values of 11.57 Ω cm and 23.7 Ω cm, respectively, along with high transparency in the visible light region of the solar spectrum and an increased carrier concentration of 3×10^{16} - 7.18×10^{19} cm^{-3} compared to undoped NiO films.[18, 19] However, the carrier

This work was supported in part by the ARENA as part of ARENA's Research and Development Program – Solar PV Research (Grant 2017/RND007) and by the Qatar National Research Fund (a member of Qatar Foundation, NPRP grant # NPRP9-021-009). (*Corresponding author: Bram Hoex*)

M. A. Hossain, T. Zhang, D. Lambert, and B. Hoex are with the School of Photovoltaics and Renewable Energy Engineering, University of New South Wales, Sydney, NSW 2052, Australia (a.hossain@unsw.edu.au, z5119402@unswalumni.com, lamberda@tcd.ie, b.hoex@unsw.edu.au).

P. A. Burr is with the School of Mechanical and Manufacturing Engineering, University of New South Wales, NSW 2052, Australia (p.burr@unsw.edu.au).

Y. Zakaria and A. Abdallah are with Qatar Environment and Energy Research Institute, Hamad Bin Khalifa University, Doha, Qatar (yzakaria@hbku.edu.au, aabdallah@hbku.edu.qa).

S. N. Rashkeev is with the Materials Science and Engineeing, University of Maryland, College Park, MD 20742 (rashkesn@umd.edu).

mobility of the K-doped NiO films is affected by the relatively large ionic radii of K^+ (1.3 Å) compared to Ni^{2+} (0.69 Å). Despite the enhancement of electrical properties, the use of alkaline metals doped NiO films in solar cells has not yet been reported.

The incorporation of Cu, Zn and Al into the NiO_x has been reported to enhance charge carrier concentrations and consequently the electrical conductivity of NiO.[4, 20] A significant increase of carrier concentration and bandgap narrowing were reported for sputtered Al-doped NiO films by Nandy *et al*.,[21]; however, a theoretical study is needed for a better understanding of the doped material. Yang *et al.*[4] showed that doping of NiO with Cu increased its work function from 4.34 eV for pure NiO to 4.58 eV, its carrier concentrations up to 1×10^{19} cm^{-3}, and conductivity up to ~50 S cm^{-1} for 27.1 at% Cu-doped NiO. Silicon solar cells with a Cu-doped NiO hole collector had a significantly lower series resistance (R_s) and saturation current density (J_0) than their counterparts with undoped NiO resulting in a champion efficiency of 9.1%.[4] These promising results suggest that even though various groups have successfully altered the electronic properties of NiO, there is still room for improvement to reach its full potential in silicon solar cells. We recently demonstrated a thermally stable Zn-doped NiO film with a low contact resistance of ~20 mΩcm^2 on c-Si, thus showing NiO-based passivity's potential hole-contacts for c-Si solar cells.[22]

NiO with an enhanced hole-conductivity and narrow VB offset with *p*-Si is needed to improve carrier separation and collection efficiency of NiO/c-Si heterojunction solar cells. First-principles density functional theory (DFT) calculations, a reliable theoretical tool that complements experiments by materials properties prediction, were carried out to identify potential dopants for increasing the conductivity of NiO. In this work, we first present DFT calculations of NiO host lattice with extrinsic W, Ta, Nb, Mo, Si, Sn, Ti, Sr, Zn, Al, Mg and Hf dopants with a particular focus on their solubility and their effect on the electronic and optical properties. We show that these metal dopants can change oxidation states with respect to the host metal cation (Ni^{2+}) of NiO and Fermi level-dependent electronic properties of the doped NiO. To the best of our knowledge, a systematic DFT defect study on NiO doping has not been reported to date. Subsequently, Al-doped NiO films of selected film compositions were synthesized onto c-Si using an atomic layer deposition (ALD) supercycle approach. The Al_xNi_yO films were found to have a low contact resistivity on c-Si contact in good agreement with the DFT calculations.

II. Methodology

A. Computational Details

The computational work was carried out by the first-principles density functional theory (DFT) approach using the projector augmented wave (PAW)[23] pseudopotentials as implemented in the Vienna Ab-initio Simulation Package (VASP).[24] For each element considered in this study, the number of valence electrons in the pseudopotentials is shown in parentheses: Ni (10), O (6), Zn (12), Al (3), Hf (12), Mg (8), Mo (12), W (12), Nb (13), Si (4), Sn (14), Sr (10), Ta (11) and Ti (12). The interaction between the valence electrons was first described by the generalized gradient approximation (GGA) as formulated in the Perdew-Burke-Ernzerhof (PBE) density functional,[24] and selected calculations were repeated with the hybrid functional of Heyd−Scuseria−Ernzerhof (HSE06).[25] A kinetic energy cutoff of 520 eV was used throughout. This yielded a total energy convergence within 1 meV, consistent with previous work on TMOs.[22, 26, 27] Integration over the Brillouin zone for the 2×2×2 NiO supercell (64 atoms) was performed using a 5×5×5 *k*-point mesh generated by within the Monkhorst-Pack scheme, with Gaussian smearing of 0.01 eV.[28] The electronic density of states (DOS) was computed using the tetrahedron scheme, and all calculations were spin-polarised because of the antiferromagnetic magnetic structure of the bulk NiO.[29] The rotationally invariant on-site Coulomb correction (GGA+U) was applied to the Ni 3d orbital using Dudarev's formalism,[30] with a U value of 5.3 eV, in line with published values.[31]

Intrinsic vacancies of nickel (V_{Ni}) and oxygen (V_O), and substitutional extrinsic dopants were considered. The defectless supercell was fully relaxed (lattice parameters and atomic positions) until the energy difference between ionic steps was below 1×10^{-6} eV, and forces on all ions were less than 1 meV/Å. The electronic convergence criteria were set to 1×10^{-8} eV. Defect calculations were performed at a constant volume (only atomic positions were relaxed) to emulate better dilute conditions. As shown in Table 1, most previous DFT studies used 32-128 atoms NiO supercells, where the choice of exchange-correlation functionals and k-points sampling were varied. Therefore, the suitability of the chosen supercell size for modelling point defects was verified by comparing the formation energy of Al_{Ni}^{q} defects (charged and charge-neutral) obtained from the 64-atom supercell with those of the 512 atoms NiO supercells. As shown in Table 2, the difference of formation energy among these supercells was reasonably small, confirming that the 64-atom supercells were adequate.[32] This was a necessary compromise in computational intensity to investigate the large set of dopants considered here in the various charge states.

Table 1. Computational parameters used for DFT modeling of NiO as reported in the literature.

Year	Level of theory	No. of atoms	k-points	E_{Cutoff} (eV)	Defects [Ref]
1999	LDA, PW91	64	4×4×4	400	Cu [33]
2007	PBE	64, 128	4×4×4, 2×2×2	400	Intrinsic [34]
2008	PBE+U (5.3 eV)	64	5×5×5	500	Intrinsic [35]
2017	PBE	32	4×4×4	520	Fe [36]

Table 2. Formation energy of Al_{Ni}^{q} in 64 and 512 atoms NiO supercells at O-rich conditions. The Fermi levels are referenced to E_{VBM} of undefective supercell for q = 0 and +1.

Size of supercells	k-points	$E^f(Al_{Ni}^{x})$ (eV)	$E^f(Al_{Ni}^{\bullet})$ (eV)
2×2×2 (64 atoms)	5×5×5	1.11	-1.81
4×4×4 (512 atoms)	1×1×1	1.31	-1.96

The formation energy $E^f(D_{Ni}^{q})$ of charged intrinsic and extrinsic defects in NiO were calculated following Eq (1),[26, 27, 37]

$$E^f(D_{Ni}^{q}) = E_{tot}^{D}(q) - E_{tot}^{host} + \sum n_i\mu_i + q(E_{VBM} + \mu_e) + \Delta^q \quad (1)$$

where $E_{tot}^{D}(q)$ represents the total energy of a defect containing NiO supercell with charge q, the E_{tot}^{host} is the energy of a perfect NiO supercell of the same size, n_i and μ_i are the number of atoms of a species i removed from or added to the

supercell, and the corresponding chemical potential of the atom, respectively. The electron chemical potential (μ_e) represents the Fermi level referenced to the valence band maximum (E_{VBM}) of an undefective NiO crystal, where μ_e was varied from 0 to the calculated bandgap energy of NiO (3.2 eV). The last term in Eq (1) represents the energy corrections needed for the charged defects to counter the self-interaction originated from the periodic boundary conditions of finite supercells. The charge states of defects were set by removing or adding electrons from the considered supercell. The Madelung potential of the 64 and 512 atoms NiO supercells was calculated to be 0.0585 eV and 0.0292 eV, respectively, using the DFT calculated macroscopic static dielectric constant ε = 5.79 which is close to the experimental value of ε = 5.7.[38] This small Madelung potential implies that the charge-charge self-interaction is small. Nevertheless, we introduced an image-charge correction to minimize the long-range Coulomb interaction for the charged defects and its periodic image. We utilized the Lany and Zunger correction,[39] calculated by non-cubic adaptation code, DeFAP, as implemented by Hine and Murphy, which is 0.65 times the Coulomb-only point charge correction schemes to account for potential alignment,[40] to the formation energy calculated using the 64 atom supercell.

The chemical potential (μ_i) of Ni, O, and extrinsic metal cations were calculated using the literature method.[26, 37] This method assumes that the transition metal dopants are in thermodynamic equilibrium with a reservoir of TMO when they are synthesized under O-rich conditions, which is the case for most NiO films. Commonly, the chemical potential of the defective species is calculated through DFT simulations of their oxide. However, these metal oxides often require an additional U parameter of a different value from that used to simulate the dopant in NiO, which causes a problem in comparing the formation energy across different phases. Instead, the chemical potential can be written in terms of the Gibbs free energy of formation of the respective binary metal oxide ($\mathrm{M_xO_y}$) in the standard growth conditions (T^0 = 298.15 K, and pO_2^0 = 1 atm), as follows:

$$\Delta \mathrm{G_f^{M_xO_y}}(p\mathrm{O_2^0}, T^0) = \mu_{\mathrm{M_xO_y(s)}} - x\mu_{\mathrm{M(s)}} - \frac{y}{2}\mu_{\mathrm{O_2}}(p\mathrm{O_2^0}, T^0) \quad (2)$$

where $\mu_{\mathrm{M(s)}}$ is obtained from the DFT calculation of the parent metal crystal (e.g., fcc Ni), and the Gibbs free energy $\Delta \mathrm{G_f^{M_xO_y}}(p\mathrm{O_2^0}, T^0)$ was taken from the standard free energy tables.[41] Compared to a gaseous phase, the dependence of a solid phase on temperature and partial pressure can be considered negligible. The chemical potential of the constituents M and O must be equal to the chemical potential of $\mathrm{M_xO_y}$; therefore, it can be written as follows:

$$\mu_{\mathrm{M_xO_y(s)}} = x\mu_{\mathrm{M(M_xO_y)}} + y\mu_{\mathrm{O(M_xO_y)}} \quad (3)$$

When the $\mathrm{M_xO_y}$ is in thermodynamic equilibrium with the environment, then the oxygen chemical potential at a temperature (T) and oxygen partial pressure ($p\mathrm{O_2}$) can be written as

$$\mu_{\mathrm{O(M_xO_y)}}(p\mathrm{O_2}, T) = \frac{1}{2}\mu_{\mathrm{O_2(g)}}(p\mathrm{O_2}, T) \quad (4)$$

From the equation (3) and (4), the μ_M at T and pO_2 can be written as:

$$\mu_{\mathrm{M(M_xO_y)}}(p\mathrm{O_2}, T) = \frac{1}{\mathrm{x}}\left(\mu_{\mathrm{M_xO_y(s)}} - \frac{y}{2}\mu_{\mathrm{O_2(g)}}(p\mathrm{O_2}, T)\right) \quad (5)$$

Combining the equation (2) and (5), the μ_{M} in $\mathrm{M_xO_y(s)}$ can be written as:

$$\mu_{\mathrm{M(M_xO_y)}}(p\mathrm{O_2}, T) = \frac{1}{\mathrm{x}}\left(\Delta \mathrm{G_f^{M_xO_y}}(p\mathrm{O_2^0}, T^0) + x\mu_{\mathrm{M(s)}} + \frac{y}{2}\mu_{\mathrm{O_2}(g)}(p\mathrm{O_2^0}, T^0) - \frac{y}{2}\mu_{\mathrm{O_2(g)}}(p\mathrm{O_2}, T)\right) \quad (6)$$

where, the $\mu_{\mathrm{O_2(g)}}$ at a nonstandard condition T and $\mathrm{p}O_2$ is obtained from the rigid-dumbbell ideal gas model.[26, 42, 43] This approach ensures the consistency of the μ_i of constituent elements for subsequent defect formation energy calculations.

B. Synthesis of the ternary Al_xNi_yO by ALD

The $\mathrm{Al_xNi_yO}$ films were synthesized by ALD onto single-side polished 500 µm thick Czochralski (Cz) Si wafers and double-side polished 180 µm thick 2.0 Ω cm *p*-type Cz Si wafers for material characterization and contact resistivity measurements, respectively. The c-Si wafers were cleaned using a standard Radio Corporation of America (RCA) cleaning with or without a final dip in 2% w/v HF solution to either remove or intentionally leave the native SiO_2 layer onto c-Si prior to the deposition of $\mathrm{Al_xNi_yO}$ films. The ultrathin native SiO_2 resulting from the RCA process acts as a nucleation site for the initial growth of the TMOs. The $\mathrm{Al_xNi_yO}$ was deposited using the ALD supercycle approach considering the growth rate per cycle (GPC) of the constituent involved oxides.[24,25] For example, to deposit the Al-doped NiO, bis-(N,N'-di-t-butylacetamidinato) nickel (II) (NiAMD), trimethyl aluminum (TMA) and H_2O were used as precursors for Ni, Al and O, respectively, at a deposition temperature of 150 °C. Based on the GPC of NiO and Al_2O_3, the ALD super-cycles was varied to obtain different Al content into the ternary NiO. An Al_2O_3 to NiO cycle ratios of 1:50, 1:25 and 1:10 were used to achieve different Al concentrations into the films.

The deposited films were characterized by spectroscopic ellipsometry (SE), X-ray photoelectron spectroscopy (XPS), ultraviolet photoelectron spectroscopy (UPS), time-of-flight secondary ion mass spectrometry (ToF-SIMS), transmission electron microscopy (TEM), energy-dispersive X-ray spectroscopy (EDS), and contact resistance measurements. The XPS measurements were conducted using Escalab 250Xi, and spectra were analyzed using the Avantage software. The hole selectivity was evaluated by using the Cox and Strack method, where Pd/Ag bilayer was deposited by e-beam and thermal evaporation, respectively. The thermal stability of the contact was measured by annealing the samples in a rapid thermal process system (RTP-600xp) in a 5000 sccm N_2 atmosphere for 10 min at different temperatures of 180 – 400 °C.

III. Results and Discussion

A. Structural properties of pure NiO

Localized d-electrons of transition metal cations result in a large local magnetic moment and magnetic ordering. At room temperature, NiO has the sodium chloride (NaCl)-type crystal structure with the space group of $Fm\bar{3}m$ where atoms are arranged in octahedral coordination and exhibits spin polarization with antiferromagnetic (AFM) ordering on the Ni sublattice, up to the Néel temperature of 523 K.[44] Two AFM structures, called AFM-I and AFM-II, following the

nomenclature of previous studies [45] were considered (Figure 1). Magnetic moments in the AFM-II structure were alternated across neighboring (111) planes. Of the two structures considered, the AFM-II resulted in the lowest energy in the DFT calculations, in agreement with the literature.[34, 46] Therefore, all further calculations were conducted considering the AFM-II NiO magnetic structure. A slight distortion of the cubic crystal lattice was also observed due to the AFM arrangement of the spin on the Ni atoms, leading to a rhombohedral lattice. This distortion is also consistent with the published literature.[46]

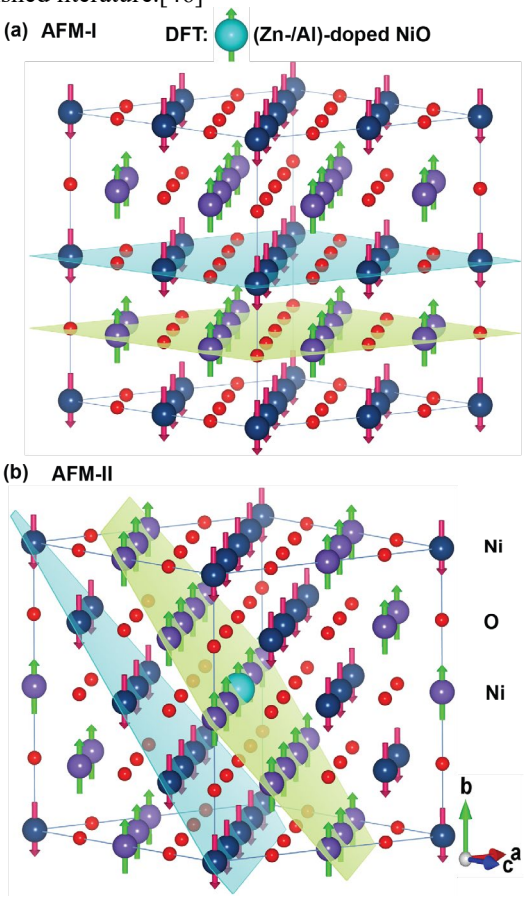

Figure 1. Magnetic ordering of a pristine NiO 2×2×2 supercell with (a) AFM-I and (b) AFM-II configurations. The translucent blue and green planes represent planes of atoms with the same spin; these are along the (100) and (111) planes for AFM-I and AFM-II, respectively.

The GGA+U calculated lattice parameters, Ni-O bond lengths, local magnetic moments, and bandgap energies of NiO are listed in Table 3. The relaxed lattice parameter for the bulk AFM-II NiO structure was found to be 4.18 Å, which matched well with an experimental lattice of 4.17 Å,[31] and with previous DFT studies. The calculated Ni-O bond length of 2.09 Å and local magnetic moment on Ni atom of 1.69 μB for the pristine NiO are also in good agreement with experimental DFT literature.[47] The calculated bandgap of 3.2 eV for the pristine NiO is smaller than its experimental counterpart of 3.6 – 4.3 eV, which is not unexpected as semi-local DFT often underestimates the bandgap of metal oxides,[48] and is corrected when a hybrid functional is used instead (4.6 eV, from our HSE06 calculations). As shown in Table 3, the structural properties of NiO from GGA+U calculations with an appropriate U parameter were comparable to data obtained from the HSE06 hybrid calculations.

Table 3. DFT calculated data compared to the experimental lattice parameter, bandgap, and local magnetic moment on Ni atoms for a perfect NiO with AFM-II structure.

	Lattice (Å)	Bandgap (eV)	Ni-O bond length (Å)	Ni magnetic moment (μB)	Ref.
This work GGA+U (5.3)	4.18	3.20	2.09	1.69	
This work HSE06	4.18	4.60	2.09	1.65	
GGA+U (5.3)	4.20	3.20		1.69	[31, 34, 36]
GGA+U (5.3)	4.19	3.53		1.67	[34]
GGA+U (5.3)	4.19	3.10		1.69	[35]
HSE06	4.18	4.10		1.66	[31]
Experiment	4.17	3.60		1.64–1.9	[49, 50]

B. Intrinsic defects properties of pure NiO

The electronic density of states (DOS) of a pristine 64 atoms NiO supercell, presented in Figure 2(a), shows that the VB predominantly consisted of O 2p and Ni-3d states and reflected the covalent bonding nature originated from significant hybridization between the Ni 3d and O 2p orbitals. However, as shown in Figure 2(b), the O 2p contribution dominated the VBM, confirming its charge-transfer and Mott-Hubbard type characteristics. A wide VB of 6.9 eV was observed, as well as a CB dominated by the Ni-3d states, both of which agree with the literature.[33],[34] As the *p*-type characteristics of NiO is resulting from its non-stoichiometry, the DFT calculations were first focused on intrinsic V_{Ni} and V_O defects to reveal the electronic properties of NiO. Interstitial defects of Ni and O are unlikely to form spontaneously because of the high defect formation energies originated from the densely packed NaCl-type structure.[35] The band structure also reveals the indirect bandgap,[51], where the bandgap was determined by the highest VB states and the lowest CB states resulting from O 2p states and Ni 3d states, respectively.

The transition level diagram (Figure 3) shows the formation energies of intrinsic V_O and V_{Ni} at various charge states under O-rich conditions. Excess oxygen in NiO is accommodated chiefly by nickel vacancies (V''_{Ni}),[52] charge-compensated by holes, resulting in a *p*-type conductivity at higher pO_2.[52] As shown in Figure 3, the formation energy of V_O ranges between 5.25 – 6.52 eV. $V_O^{\bullet\bullet}$ is more stable at low Fermi levels, transitioning to $V_O^{\bullet}$ at E_f = 0.12 eV and then charge-neutral oxygen vacancy ($V_O^{\times}$) at E_f = 1.15 eV. While $V_O^{\bullet\bullet}$ and $V_O^{\bullet}$ defects are expected to experimentally form at low Fermi energies (≤1.15 eV), the $V_O^{\times}$ can only be stable at high Fermi energies (Figure 3). It is worth to point out that irrespective of charge states, all V_O are highly unfavourable and experimentally least expected to be observed under the O-rich conditions.

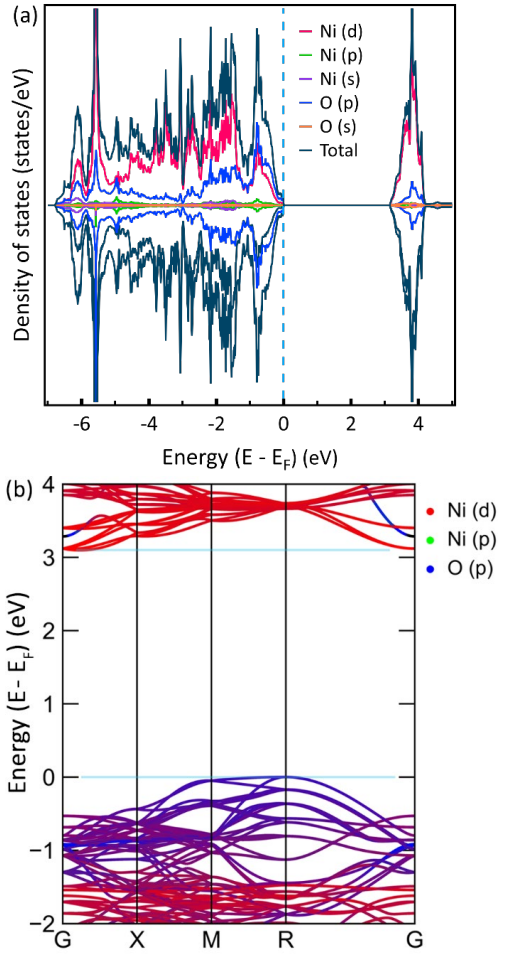

Figure 2. Calculated (GGA+U) electronic structure of pristine NiO. (a) Spin-polarised total and species-projected DOS where the dashed vertical line indicates the Fermi energy. (b) corresponding band structure.

As shown in Figure 3, V_{Ni} was the predominant intrinsic defect under O-rich conditions. At Fermi levels above 1 eV, V_{Ni} was fully charged V_{Ni}''.[53-55] However, the neutral ($V_{Ni}^{\times}$) and +1 charge states V_{Ni}' were stable up to 0.32 eV and 1.05 eV with respect to the VBM, respectively (Figure 3). The slightly lower $V_{Ni}^{\times}$ formation energies of 0.32 eV compared to previously reported (0.48 eV),[48] was believed to arise from the size of supercell and choice of using Gibbs free energy at standard conditions to calculate the chemical potential of constituent elements nickel and oxygen. The negative energies for V_{Ni}' and V_{Ni}'' defect formation indicate that these native defects are easier to form compared to the charge-neutral $V_{Ni}^{\times}$ in identical growth conditions. The formation energies are particularly sensitive to the DFT description of O_2 gas molecules, sometimes used to define the chemical potential for O. Therefore, we used the standard Gibbs free energies of formation of NiO to calculate chemical potential and consequently the formation energy of the defect species in NiO. This reduces the sensitivity of the results on the DFT simulation parameters.[26, 42]

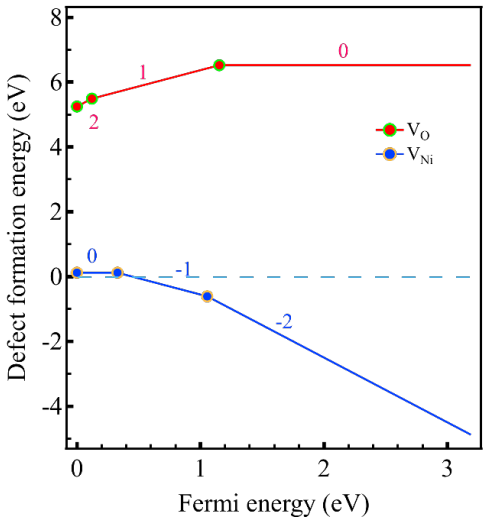

Figure 3. Transition level diagram shows calculated formation energies of intrinsic defects as a function of Fermi energy within the bandgap of NiO at O-rich growth condition. The oxygen chemical potential was -2.58 eV (i.e. standard conditions of 298.15 K and pO_2 = 0.2 atm). The lowest energy charge states at the Fermi level are labeled, and filled circles indicate the transition levels.

As the growth of materials depends on the deposition conditions, the intrinsic defects, V_O (Figure 4a) and V_{Ni} (Figure 4b) were first considered. The DOS of pure NiO shows no defect states within the bandgap (Figure 2a). However, the intrinsic V_O and V_{Ni} induce defect states within the NiO bandgap and their position changes with defect charge. The $V_O^{\times}$ in NiO leads to the formation of two defect levels resulted from the structural geometry optimization: a filled defect state at 1 eV above the VBM and another empty defect level 0.3 eV below the conduction band minimum (CBM), indicating a donor-type electronic structure. The electrons around $V_O^{\times}$ can be excited to the CB. The dominating defect states close to the CBM originate from the Ni 3d orbital, and the one close to the VBM is contributed mainly by O-2p orbital contribution. These impurity states result from dangling bonds of Ni, which are a coordinating oxygen vacancy site. A singularly charged oxygen vacancy, $V_O^{\bullet}$, appeared spin-polarized with the splitting of both defect states, and only the lowest state occupied, and empty deep defect bands at 0.8 eV above Fermi level in spin-up states is deep trap states while two shallow defects levels with spin-up and spin-down states were observed close to the CB edge. The empty defect bands for the $V_O^{\bullet\bullet}$ defects were close to the CBM. However, as suggested by the formation energy (Figure 3) it was unstable at a high Fermi level under the O-rich condition.

For typical growth conditions, NiO shows *p*-type conductivity due to the presence of V_{Ni}, which is the predominant and most stable defect under the O-rich conditions. As shown in Figure 4b, the empty states created by the V_{Ni} were shallow and closer to the VB of c-Si, thereby participating in hole conduction through these shallow states of NiO. It is understood that the V_{Ni}^{x} defects create dangling oxygen bonds, which result in localized defect states. These trap states were within a shallow defect level, approximately 0.3 eV above the VBM of NiO, in close agreement with the experiments by Flynn *et al.*,[56, 57] which showed that these defects associated with V_{Ni} are located at 0.4 eV above the

VBM. Oxygen atoms around $V_{Ni}^{\times}$ and nickel atoms around $V_{O}^{\times}$ in their relaxed NiO structure were found to move outward by 8%, and inward by 3%, respectively (Figure S2).

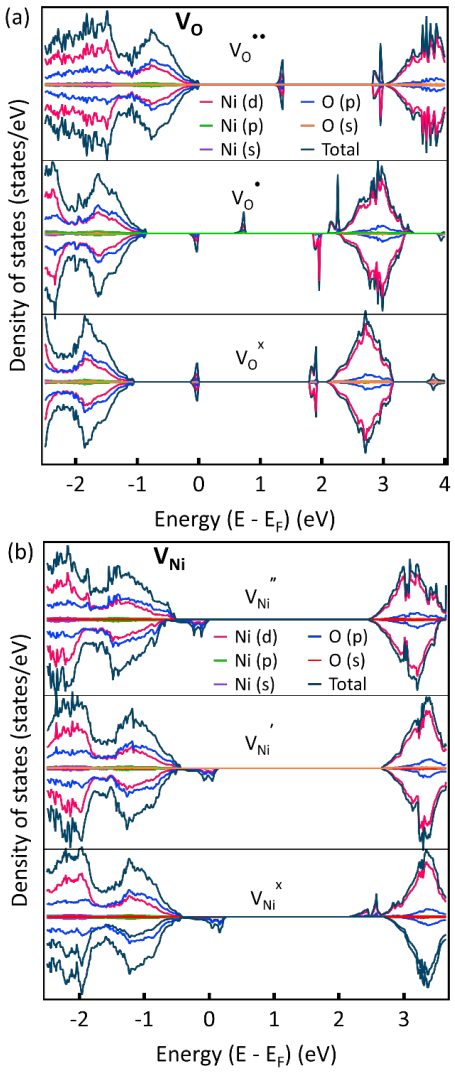

Figure 4. Calculated spin-polarized total and species-projected DOS plots of NiO containing (a) an oxygen vacancy and (b) a nickel vacancy. The Fermi level was set to zero.

C. Doping of NiO with metals

The electrical conductivity of TMOs can vary from insulating to semiconducting to metallic based on their doping asymmetry characteristics and capability to accommodate various types of defects. Most TMOs suffer from insufficient electrical conductivity for application in solar cells and electrocatalysis. Incorporation of multivalent transition metal cations could be a viable approach to transform NiO from insulating to semi-metallic upon partially filling the *d*-orbital and change of cation oxidation states. The changeable oxidation states of metal dopants could result in favorable gap states within NiO, creating pathways for charge transport, thus enhancing the electrical conductivity of NiO. Knowing the solubility limit of these metal cations in NiO is important for obtaining a single-phase material with enhanced charge-carrier dynamics.

As this study focuses on typical substitutional extrinsic defects of commonly used atomic layer deposition (ALD) metal precursors, the following dopants were considered, and their effect on the electronic properties of NiO was predicted using DFT calculations: W, Ta, Nb, Mo, Si, Sn, Ti, Sr, Zn, Al, Mg and Hf. Eq (6) was used to calculate the chemical potential of these dopants where Gibbs free energy at standard condition was used for the respective stable metal oxides of WO_3, Ta_2O_5, Nb_2O_5, MoO_3, SiO_2, SnO_2, TiO_2, SrO_2, ZnO, Al_2O_3, MgO and HfO_2.[41] The transition level diagram (Figure 5) shows formation energies of extrinsic defects at the most favorable charge states at standard conditions of 298.15 K and pO_2 = 0.2 atm.

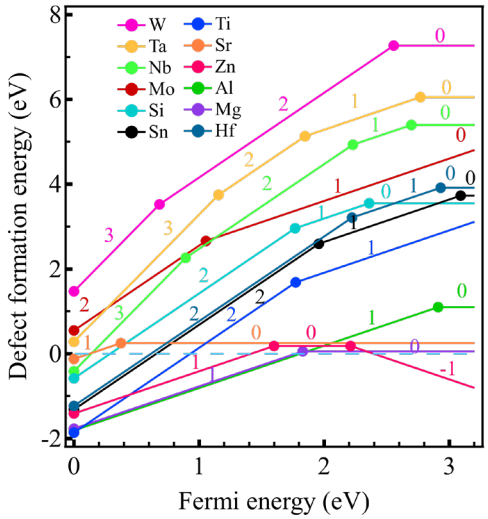

Figure 5. The GGA+U calculated formation energies of substitutional extrinsic defects as a function of Fermi energy within the bandgap of NiO at O-rich growth condition. The VBM is set at 0 eV. The lowest energy charge states at the Fermi level are labelled in numbers, and filled circles indicate the charge transition levels.

The synthesis and subsequent post-deposition temperature and pO_2 have a significant impact on the stability of the final structure of ternary NiO. Controlling the defects' chemistry and charge states of materials is crucial because it leads to potential applications. For instance, increasing conductivity by introducing shallow defect states is required for solar cells and enhancing surface defects required for potential electrocatalyst applications. As shown in Figure 5, the investigated extrinsic defects are predicted to be often accommodated as charged defects. For example, the charge-neutral state of $Ta_{Ni}^{\times}$ defect possesses a higher defect formation energy and is only stable at a higher Fermi level compared to the charged defects of $Ta_{Ni}^{\bullet\bullet\bullet}$, $Ta_{Ni}^{\bullet\bullet}$, and $Ta_{Ni}^{\bullet}$ (equivalent to Ta cations in 5+, 4+ and 3+ oxidation states, respectively, on the Ni^{2+} lattice site).

Figure S1 shows the total spin-up DOS of all the doped NiO supercells considered here and in all charged states (including those that do not exhibit a stable regime in Figure 5). The total spin-up DOS of the pristine NiO is also shown for comparison. While most of the dilute dopants introduce bandgap defect states (*i.e.,* $Ta_{Ni}^{\bullet\bullet\bullet}$, $Zn_{Ni}^{\bullet}$, $Al_{Ni}^{\bullet}$, $Mg_{Ni}^{\bullet}$, $Hf_{Ni}^{\bullet\bullet}$, $Ti_{Ni}^{\bullet\bullet}$, $W_{Ni}^{\bullet\bullet\bullet}$, $Nb_{Ni}^{\bullet\bullet\bullet}$, $Mo_{Ni}^{\bullet\bullet}$, $Sn_{Ni}^{\bullet\bullet}$, $Si_{Ni}^{\bullet\bullet}$ and $Sr_{Ni}^{\bullet}$), some of the substitution defects in their fully charged valence state (*i.e.* $Zn_{Ni}^{\bullet}$, $Al_{Ni}^{\bullet}$, $Hf_{Ni}^{\bullet\bullet}$, $Sn_{Ni}^{\bullet\bullet}$, and $Sr_{Ni}^{\bullet}$) do not create defect states in the bandgap. These dopant defects in their lower charge states, however, show multiple defect energy levels (*i.e.,* $Nb_{Ni}^{\times}$, $W_{Ni}^{\times}$, $Ta_{Ni}^{\times}$, $Mo_{Ni}^{\times}$, $Si_{Ni}^{\times}$, $Al_{Ni}^{\times}$, $Hf_{Ni}^{\times}$,), confirming that some of these defects could play some roles in charge carriers transport pathways, provided that they

are stable at relatively low Fermi energies. Some dopants, including W, Mo, and Ta, exhibit positive formation energy at all Fermi levels, implying that these are difficult to incorporate into NiO. On the other hand, a few defects, such as Al, Sr Nb, Si, Sn, Ti and Zn, exhibit negative formation energy when the Fermi level is close to the VBM, indicating a high solubility at Fermi energies. Singly charged $Sr_{Ni}^{\bullet}$ is more easily accommodated at a low Fermi level, but the neutral charge state dominates most electron energies in NiO bandgap. The bandgap energy also reduces with some elemental doping; for example, Sr doping causes a decrease of NiO bandgap, consistent with published data in the literature.[58] $Al_{Ni}^{\bullet}$ is the more easily accommodated compared to $Al_{Ni}^{\times}$ for most of the fermi energy range. Defects, such as W_{Ni}^{q}, Ta_{Ni}^{q}, and Mo_{Ni}^{q} exhibit unfavorable formation energies compared to other defects, such as Si_{Ni}^{q}, where q denotes the Fermi level-dependent charge states. While the +4 and +3 charge states were expected for Mo_{Ni}^{q}, it appears that Mo_{Ni}^{q} only adopts a +2 and +1 charge state.

D. Hybrid DFT calculations for doped NiO

At first, the GGA+U method was used to address the spurious self-correlation of *d* and *f* electrons of transition metals, resulting in incorrect DOS values. However, some delocalization could still occur because of the lack of universality of the GGA+U method.[59] In addition, a higher U value could lead to the deterioration of other materials properties. The use of hybrid functionals prevents delocalization and produces more accurate electronic bandgap and electronic states because they enable orbital dependent nonlocal exchange correlation potential. However, it is impractical to perform geometry relaxations for large supercells. Because of computationally expensive hybrid calculations, the scaled hybrid method [26] was used to calculate DOS for the most promising defect states instead of a full atomic relaxation using HSE06.

As shown in Figure 6, the HSE06 calculated defect formation energies were different to those obtained with the GGA+U approach, presented in Figure 5. The obvious difference is the energy gap which is larger for the hybrid calculated NiO. While a large U value applied to Ni in the GGA+U could result in bandgap energies close to the experiments, Ni magnetic moment and structural properties could be compromised when a very large unphysical U parameter is used. In addition, determining the relative energetic positions of dopant states compared to the host lattice is problematic in the GGA+U approach. For example, as shown in Figure 5, while $Al_{Ni}^{\bullet}$ is stable up to 2.8 eV within the GGA+U calculated bandgap energy of 3.2 eV; however, it is stable up to the Fermi energy of 3.8 eV within the hybrid DFT calculated bandgap energy of 4.6 eV (Figure 7). Subsequently, a change in formation energies of dopants at their various charge states aswas oberverd between the GGA+U and hybrid DFT approaches. As the hybrid approach results in more accurate bandgaps and positions of dopant states, the hybrid approach was also used to compare the dopants study with the GGA+U approach. The thermodynamic transition level diagram shows that the formation energies for Mg and Zn were low across the wide range of Fermi energies in their charge-neutral states. The $Ti_{Ni}^{\bullet\bullet}$ is dominant up to the Fermi energy of 2.4 eV while the $Ti_{Ni}^{\bullet}$ is close to the conduction band, suggesting that the latter is a donor defect. It also shows that W and Sn cannot be incorporated into NiO because of high defect formation energies.

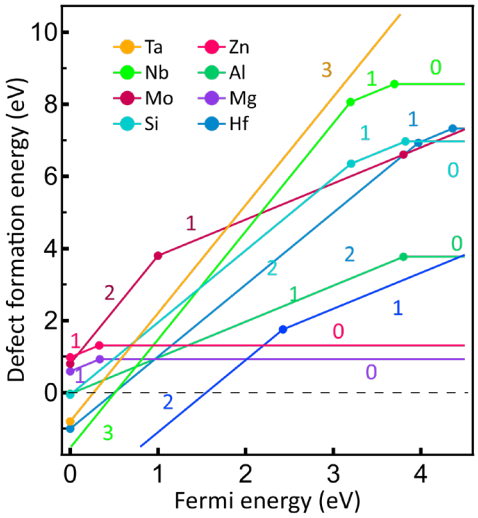

Figure 6. Hybrid DFT (HSE06) calculated formation energies of substitutional defects as a function of Fermi energy within the bandgap of NiO at O-rich growth condition.

The total DOS calculated using the hybrid method showed that defects states created by Mo_{Ni}^{q} at 0.4 eV, 1.2 eV and 1.5 eV for +2. +1 and neutral charge states, respectively, were closer to the VBM [Figure 7(a)] compared to that of the GGA+U [(Figure S1(a)] with values of 1.4 eV, 2.0 eV, and 2.2 eV, confirming the qualitative difference between the formation energies for the two approaches. As shown in Figure 7, doping of NiO leads to the formation of several states in NiO bandgap, where dopant-derived states often show a difference in the spin up and spin down, which results in a magnetic moment. A smaller Al-O bond length of 1.84 Å was observed for Al-doped NiO compared to the Ni-O bond length of 2.09 Å for pure NiO (Table 3), revealing that the Al at Ni site has a significant influence on the lattice, which could originate from the different valency of Al (+3) than the Ni (+2). The effective charge of a substitutional Al at Ni site is positive, which electrostatically attracts the negatively charged oxygen atoms, resulting in relaxation of the structure with a smaller Al-O bond length around the Al defect (Figure S3). The previous analysis using GGA+U, presented in Figure S1(b), of Al-doped NiO showed empty defect states in the bandgap for $Al_{Ni}^{\times}$ which were only stable at very high Fermi levels. Al incorporation has been reported to enhance the electrical conductivity of NiO.[4, 20, 21]

The HSE06 results show that the charge-neutral $Al_{Ni}^{\times}$ dopant leads to the formation of several states in the bandgap (close to VB and in mid bandgap), both in agreement with the GGA+U calculations shown in Figure S1(b). The $Al_{Ni}^{\times}$ results in defects states in the bandgap of NiO created by 2+ oxidation state of Al, which likely to occur only at high Fermi levels, as shown in Figure S1(b). These dopant-derived DOS show a small excess of spin-up over spin-down states and form the highest occupied states, lying below the Fermi level of the Al-doped NiO. These mid-gap states of $Al_{Ni}^{\times}$ act as Shockley-Read-Hall (SRH) carrier recombination centres to trap photogenerated charge carriers and are not expected in solar cell applications. The reduction of

NiO bandgap upon Al doping could arise from unoccupied dopant-induced states above the highest occupied state, resulting in a narrow bandgap for the Al-doped NiO. The unoccupied Ni 3d state at the bottom of the CB for the $Al_{Ni}^{\bullet}$ suggest that Ni contributes to the gap states. However, Al_{Ni} is stable as a positively charged $Al_{Ni}^{\bullet}$ for most of the Fermi levels up to 2.8 eV, and results in defect levels close to the band edge. In this regime, the defect states close to the CBM of NiO are expected to work as a shallow donor defect because of the free electron released to CB resulting from the replacement of Ni^{2+} by Al^{3+}. At higher concentrations, the defect-defect interactions might create deep level defect states within the bandgap. This is not investigated here as the simulations represent dilute defects with an effective concentration of 3.12 at% dopants.

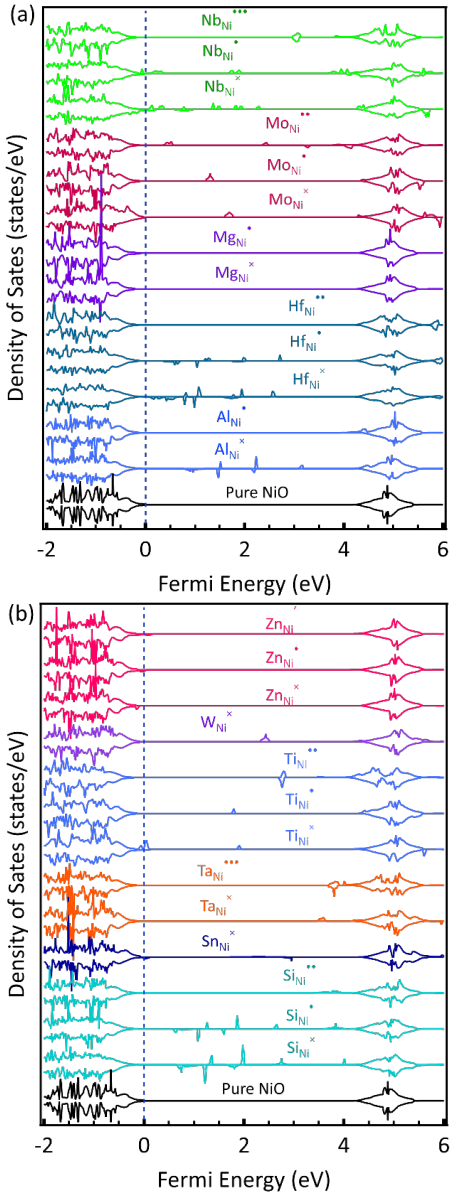

Figure 7. HSE06 spin-polarised total DOS of the NiO with dopants in various charged states (a, b). Total DOS of a pristine NiO is also provided for comparison. As the core states are not affected by the presence of defects, all energies are aligned to the O (s) core states of the pristine NiO structure.

The defects such as Hf, Ti, Mo, Si are expected to act as donor defects at high Fermi energies, but the multivalent dopants, such as Al, Si, Ti, Mo, Nb, and Hf create defect states close to the NiO VB, are expected to act as a photogenerated charge carrier transport pathway from c-Si to the contact in a c-Si solar cell; thus, improving its charge collection efficiency.

E. Experimental synthesis of Al-doped NiO by ALD

As shown in Figure 5 and Figure 6, the DFT analyses show that $Al_{Ni}^{\bullet}$ is more stable than $Al_{Ni}^{\times}$ up to a Fermi energy of 2.7 eV for GGA+U and 3.8 eV for hybrid calculations. Figure S1 and Figure 7 show that the defect states introduced by $Al_{Ni}^{\bullet}$ are close to the band edges. Therefore, these defect states of Al-doped NiO could act as transport pathways of the photogenerated charge carrier from c-Si to the metal contact, suggesting potential conductivity improvements for the Al-doped NiO films. Therefore, approximately 8.5 nm thick Al_xNi_yO films were synthesized by ALD. The electronic structure and chemical composition of the Al_xNi_yO films deposited onto c-Si/SiO_2 substrate and the interface composition in c-Si/SiO_2/Al_xNi_yO stack layers were analyzed by XPS surface and depth profiling measurements, respectively. Three Al_xNi_yO films showed an increasing concentration of Al with increasing Al_2O_3 cycles in the Al_2O_3:NiO ALD supercycles. The Al concentration in these films was estimated to be higher than that of the Al_2O_3:NiO ALD supercycles ratios of 1:50, 1:25 and 1:10, resulting from much higher growth per cycle of the Al_2O_3 than NiO during growth by ALD (Table 4).[60]

Table 4. The atomic composition of the Al-doped NiO samples deposited by ALD determined by XPS.

ALD super-cycle ratio Al_2O_3:NiO	Ni 2p (at %)	O 1s (at %)	Al 2s (at %)	C 1s (at%)	Formula
1:50	30.3	45.7	8.6	15.4	$Al_{0.21}Ni_{0.75}O$
1:25	22.3	48.3	13.8	15.6	$Al_{0.32}Ni_{0.52}O$
1:10	14.8	49.2	19.1	16.9	$Al_{0.44}Ni_{0.34}O$

As shown in Table 4, XPS revealed the stochiometry of Al_xNi_yO films as $Al_{0.21}Ni_{0.75}O$, $Al_{0.32}Ni_{0.52}O$ and $Al_{0.44}Ni_{0.34}O$ with increasing NiO supercycles. The deposited Al_xNi_yO films contain significantly more Al as would be expected from the ALD supercycle ratio. This is due to a significantly lower growth per cycle of NiO vs Al_2O_3 and some nucleation delay for the deposition of ALD NiO. This was also reported by Baker *et al.*[60] who reported a significantly higher uptake of Al than Ni towards the formation of Al_xNi_yO from their binary Al_2O_3 and NiO ALD cycles, confirming a nickel deficient (Al-rich) Al_xNi_yO films. The Al_xNi_yO films showed the presence of two types of bonded nickel ions (Figure 8a), such as Ni^{2+} and Ni^{3+} states, with the characteristic peak binding energies of 854.4 eV and 855.7 eV,[10] respectively, suggesting the presence of NiO and Ni_2O_3 in the as-deposited Al_xNi_yO films. Luca *et al.*[61] have shown that the formation energies for these oxides are close, resulting in the decomposition of the Ni_2O_3 into more stable NiO based on the temperature and pressure. The presence of Ni^{3+} is an indirect indication of the presence of V_{Ni} into the NiO films because dangling bonds created by V_{Ni} interact with Ni 3d electrons and cause the loss of an electron from neighboring Ni^{2+} atoms. Therefore, to maintain charge neutrality, two neighboring Ni^{2+} are oxidized to Ni^{3+}, resulting in the release of a hole into the VB. It is worth noting that $Al_{Ni}^{\bullet}$ (Al^{3+}) would also act a charge-compensating species for V_{Ni}'', suggesting that the addition of Al should reduce the amount of

Ni^{3+} and increase the amount of V_{Ni}''. Therefore, Al^{3+} and Ni^{3+} are competing defects, where the former one helps creating more V_{Ni}''; thus, resulting in an increase of p-type conductivity for higher concentration of Al as shown in contact performance measurements on c-Si.

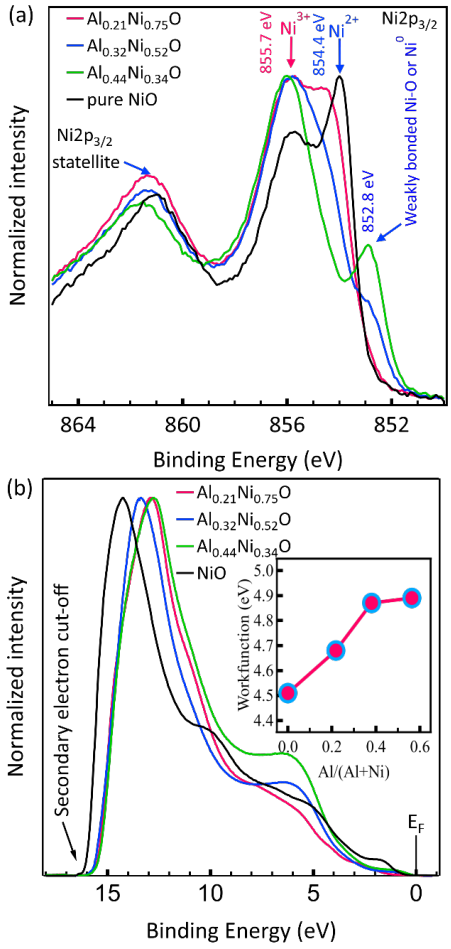

Figure 8. (a) XPS spectra of the Ni $2p_{3/2}$ peaks of the $Al_{0.21}Ni_{0.75}O$, $Al_{0.32}Ni_{0.52}O$, $Al_{0.44}Ni_{0.34}O$, and pure NiO films, which show a shift of the spectra towards higher energy with the increase of Al content. (b) UPS spectra of the films. Inset Figure shows the calculated work functions of the ALD deposited NiO and Al_xNi_yO films with different Al/(Al+Ni) ratio.

The deconvoluted O 1s spectra show a peak binding energy (BE) of 529.9 eV corresponding to the presence of Ni^{2+} (NiO), and the peak BE around 531.1 eV confirms lattice oxygen associated with the Ni-O and Al-O bonds [Ni^{3+}, Al_2O_3 and AlO(OH)] (Figure S4). The peak binding energy 852.8 eV of the Ni $2p_{3/2}$ spectra for the high Al-containing film can be attributed to Ni^0 or weakly bonded Ni-O (Figure 8a). The peak intensity increases with the increase of Al concentration, which can also be attributed to Al-Ni bonding, suggesting that the Al-doped NiO films are more oxidized compared to pure NiO. The peak binding energy of 74.0 eV for Al $2p_{1/2}$ and the absence of the peak at 71.9 eV for metallic Al 2p (Figure S5) further confirm the incorporation of Al^{3+} into NiO.[21] The UPS analyses (Figure 8b) show a shift in the valence band of NiO with respect to the Fermi level, which could be explained by the incorporation of an increasing concentration of Al^{3+} states in the NiO films with the progressive Al incorporation. The work functions of the pure NiO, $Al_{0.21}Ni_{0.75}O$, $Al_{0.32}Ni_{0.52}O$ and $Al_{0.44}Ni_{0.34}O$ films were measured to be 4.51, 4.68, 4.87 and 4.89 eV, respectively, suggesting an increase of p-type characteristics upon Al incorporation. The work function of NiO typically ranges from 4.4 – 5.6 eV depending on their surface composition and crystalline orientation.[62]

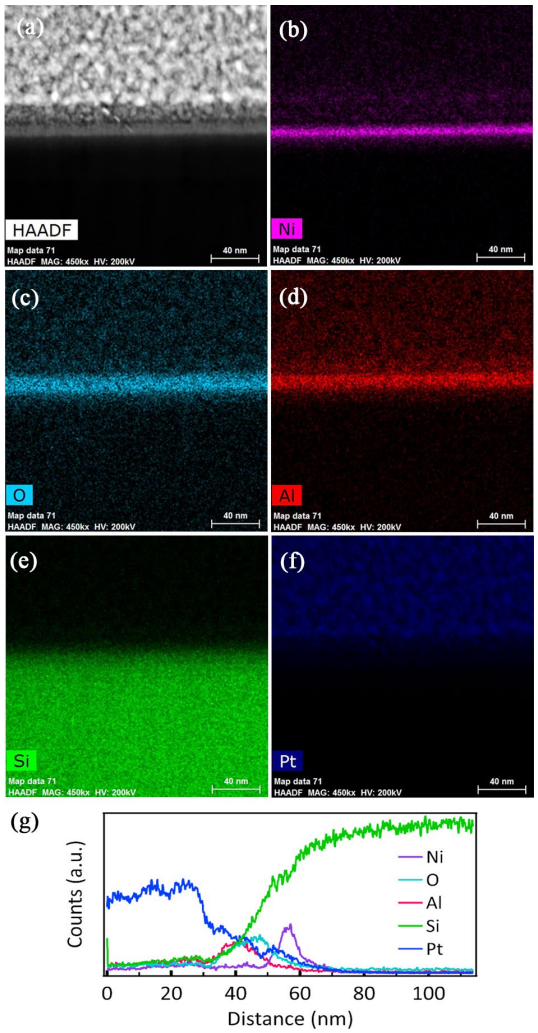

Figure 9. Shows (a) HAADF, and EDS maps of (b) Ni, (c) O, (d) Al, (e) Si and (f) Pt, and (g) corresponding EDS elemental line scan of the c-$Si/SiO_2/Al_{0.44}Ni_{0.34}O$ film.

The cross-sectional images of c-$Si/SiO_2/Al_{0.44}Ni_{0.34}O$ film were analyzed by HRTEM and EDS elemental mapping (Figure 9). The EDS mapping of the cross-sectional film shows the elemental Ni, O and Al distribution in c-$Si/SiO_2/Al_{0.44}Ni_{0.34}O$ sample. The EDS line spectra revealed detailed chemical information across the film cross-section, for example, an apparent increase in Ni signal below the O signal suggested the diffusion of the Ni through the oxide layers towards the c-Si/SiO_2 interface. However, it is worth noting that the elemental signals from EDS were strongly affected by the composition of the films as for a given electron beam intensity, light elements such as O, Al and Si emit less K_α photons while heavy elements, such as Zn and Ni emit more. Therefore, these films were further investigated with ToF-SIMS and XPS depth profiling measurements (Figure 9).

The ToF-SIMS profiles show constituent elements Ni, O, and Al in the c-$Si/SiO_2/Al_xNi_yO$ stack layers and their variation with sputter time [Figure 10(a)] which was further verified by the XPS depth profiling measurements [Figure 10(b)]. A similar

trend was observed for the $Al_{0.21}Ni_{0.75}O$ and $Al_{0.32}Ni_{0.52}O$ films (Figure S6). These results demonstrate a homogeneous distribution of constituent elements across the film thickness. The increase of Si intensity with sputter/etch time reveals a 1 nm thin SiO_2 layer, indicated by the shaded area, originated from the RCA process prior to ALD. The ToF-SIMS profiles indicate the presence of hydrogen resulting from incomplete combustion of the ALD precursors.

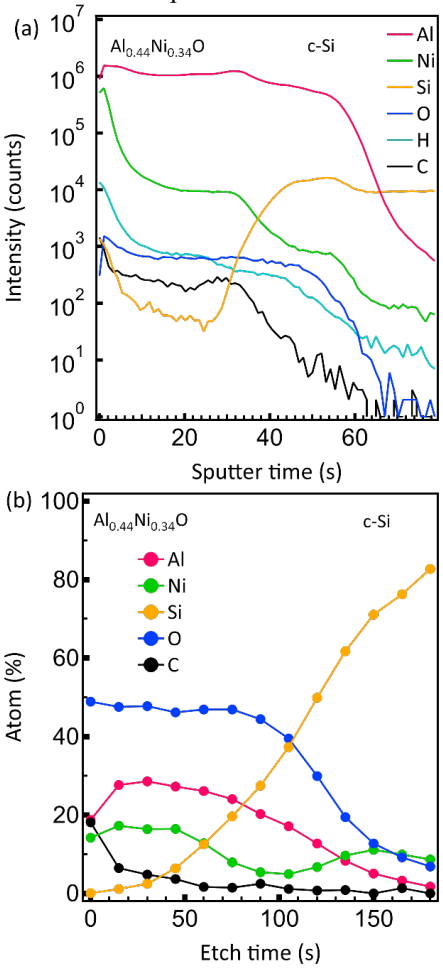

Figure 10. (a) ToF-SIMS elemental depth profiles of the $Al_{0.44}Ni_{0.34}O$ film as a function of the sputtering time and (b) elemental quantification of the film by XPS depth profiling. Based on the composition, the various layers of the sample are indicated in the figure to assist the reader.

F. Contact performance of the Al_xNi_yO films with c-Si

As mentioned in the introduction, undoped NiO does not provide an ohmic contact on c-Si (Figure S7). A contact resistivity (ρ_c) with a minimum value of ~374 mΩ cm^2 was obtained for the as-deposited $Al_{0.44}Ni_{0.34}O$ film. This significantly reduced contact resistivity compared to undoped NiO is likely caused by the energy level of the shallow defects of $Al_{Ni}^{\bullet}$ within the bandgap, as suggested by the DOS. Pure NiO tends to crystallize at the ALD growth temperature of 150 °C, often detrimental to the passivating contact performance. Therefore, the films were subsequently annealed at 200-500 °C using the rapid thermal annealing (RTA) process in N_2 gas for 10 minutes. While the low Al-content films, $Al_{0.21}Ni_{0.75}O$ and $Al_{0.32}Ni_{0.52}O$, did not show a significant improvement of the contact resistivities (>500 mΩ cm^2) after the RTA treatment, the $Al_{0.44}Ni_{0.34}O$ films did show a decrease in contact resistivity with a ρ_c value of 113 mΩ cm^2 and 41.6 mΩ cm^2 after 250 °C and 300 °C annealing [Figure 11(b)], respectively. A rapid increase of the carrier concentration and a decrease of NiO resistivity were previously reported by a higher concentration of Al^{3+} dopants, which releases an electron in the CB of NiO.[63] In addition, a higher concentration of Al reduces the crystallinity of the Al-doped NiO films.[64] These results suggest that the addition of Al in NiO keeps the film amorphous at higher annealing temperatures, which is desirable for a low contact performance. We previously demonstrated contact resistivity values of 59.3 mΩcm^2 and 21.5 mΩcm^2 for c-Si/$Zn_{0.62}Ni_{0.38}O$ in the as-deposited state and after annealing at 200 °C, respectively, and the films were thermally stable up to 500 °C.[22]

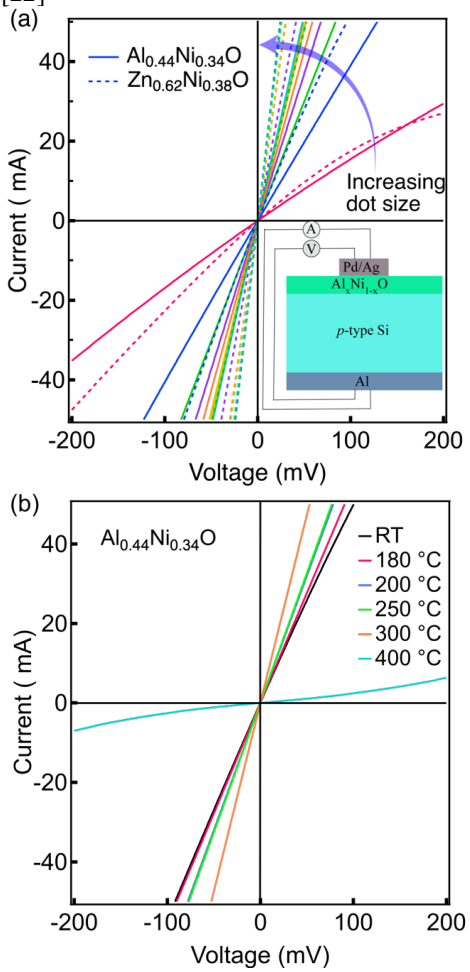

Figure 11. Dark *I-V* characteristics of p-type c-Si/$Al_{0.44}Ni_{0.34}O$ contacts (solid lines) measured in the Cox and Strack structure (inset image) using (a) Pd/Ag bilayer pads of 0.1 – 1 cm diameter circles, contact performance of c-Si/$Zn_{0.62}Ni_{0.38}O$ (dotted lines) is also shown for comparison, and (b) post-deposition annealing of the stack layer with 1 cm diameter Pd/Ag bilayer pad at 180 – 400 °C, indicating a stable ohmic c-Si/$Al_{0.44}Ni_{0.34}O$ contact, where RT is room temperature.

The effect of Al incorporation into NiO and consequent change of composition and contact performance of the films can be attributed to the deficiency of Ni in the top layer of the as-grown films as shown by the TEM EDS mapping and ToF-SIMS and XPS depth profiles. In metal oxides, both anion and cation deficiency increase conductivity, and the latter case has been observed for the as-deposited samples. Here, the contact performance of the c-Si/SiO_2/Al_xNi_yO stack improved because of an increased conductivity of the Al_xNi_yO films. This shows

that the improved contact performance of the doped NiO originated from higher conductivity as an interfacial layer with enhanced electrical conductivity plays a crucial role in obtaining improved contact performance. The addition of more Al tends to disrupt the crystallization of NiO, which would otherwise be crystalline at the ALD growth conditions. The crystallization step during the post-processing could be responsible for the reduced contact resistivity of the low Al-containing films. These results agree well with the enhanced contact performance, as shown in Figure 12. After annealing at temperatures higher than 400 °C, however, the films were unstable, which could either result from the crystallization of the deposited films or the release of hydrogen, affecting the contact performance of the deposited materials.

IV. Conclusion

In this work, we first systematically investigated the effects of intrinsic and extrinsic defects in NiO by density functional theory (DFT) calculations and demonstrated how they result in defect states within the bandgap and close to the valence band of NiO. We used standard and hybrid DFT approaches to investigate and obtain suitable dopants for NiO. It was shown that intrinsic nickel vacancy defects are predominant and result in p-type conductivity; however, their density is insufficient high for an effective hole-contact with p-type c-Si. Guided by the DFT calculations, Al-doped NiO films were deposited by ALD and characterized before use as hole-selective contact with c-Si and compared with Zn-doped NiO films. The bandgap of the Al_xNi_yO films was observed to reduce upon Al-incorporation and demonstrated reasonably good ohmic contact on a p-type c-Si substrate. The contact resistivity of the $Al_{0.44}Ni_{0.34}O$ film was significantly reduced upon post-deposition annealing of the films at 180–400 °C. The obtained minimum contact resistivity value of 41.6 mΩ cm^2 for p-type c-Si/$Al_{0.44}Ni_{0.34}O$ is slightly higher than our previous work on c-Si/$Zn_{062}Ni_{0.38}O$ contact, which showed a minimum resistivity value of 21.5 mΩ cm^2. The higher contact resistivity of c-Si/$Al_{0.44}Ni_{0.34}O$ could arise from the trapping of holes in the mid-bandgap states. Therefore, this work demonstrates the potential of using doped NiO with Al, Zn, Ti, Mo, Nb and Hf dopants for tailoring carrier selective contact properties of crystalline silicon solar cells, which is crucial to obtain improvement in charge carrier separation efficiency.

Acknowledgment

Authors would like to acknowledge the computational resources from the research computing group at Texas A&M University in Qatar. This research/project was also undertaken with the assistance of resources and services from the National Computational Infrastructure (NCI), which is supported by the Australian Government, and through the UNSW-NCI partner trial scheme. The views expressed herein are not necessarily the views of the Australian Government and the Australian Government does not accept the responsibility for any information or advice contained herein.

References

[1] M. Gong *et al.*, "Nanoscale nickel oxide/nickel heterostructures for active hydrogen evolution electrocatalysis," *Nat. Commun.,* Article vol. 5, p. 4695, 08/22/online 2014, doi: 10.1038/ncomms5695 https://www.nature.com/articles/ncomms5695#supplementary-information.

[2] Q. Fu *et al.*, "Synthesis of uniform porous NiO nanotetrahedra and their excellent gas-sensing performance toward formaldehyde," *RSC Adv.,* 10.1039/C7RA10730G vol. 7, no. 82, pp. 52312-52320, 2017, doi: 10.1039/C7RA10730G.

[3] Z. Hu *et al.*, "Sol-gel-processed yttrium-doped NiO as hole transport layer in inverted perovskite solar cells for enhanced performance," *Appl. Surf. Sci.,* vol. 441, pp. 258-264, 2018/05/31/ 2018, doi: https://doi.org/10.1016/j.apsusc.2018.01.236.

[4] X. Yang, J. Guo, Y. Zhang, W. Liu, and Y. Sun, "Hole-selective NiO:Cu contact for NiO/Si heterojunction solar cells," *J. Alloy. Compd.,* vol. 747, pp. 563-570, 2018/05/30/ 2018, doi: https://doi.org/10.1016/j.jallcom.2018.03.067.

[5] J. Bullock *et al.*, "Dopant-Free Partial Rear Contacts Enabling 23% Silicon Solar Cells," *Adv. Energy Mater.,* vol. 9, no. 9, p. 1803367, 2019, doi: doi:10.1002/aenm.201803367.

[6] W. Chen, F.-Z. Liu, X.-Y. Feng, A. B. Djurišić, W. K. Chan, and Z.-B. He, "Cesium Doped NiOx as an Efficient Hole Extraction Layer for Inverted Planar Perovskite Solar Cells," *Adv. Energy Mater.,* vol. 7, no. 19, p. 1700722, 2017, doi: doi:10.1002/aenm.201700722.

[7] F. Safari-Alamuti, J. R. Jennings, M. A. Hossain, L. Y. L. Yung, and Q. Wang, "Conformal growth of nanocrystalline CdX (X = S, Se) on mesoscopic NiO and their photoelectrochemical properties," *Phys. Chem. Chem. Phys.,* 10.1039/C3CP43613F vol. 15, no. 13, pp. 4767-4774, 2013, doi: 10.1039/C3CP43613F.

[8] P. Yang, X. Tong, G. Wang, Z. Gao, X. Guo, and Y. Qin, "NiO/SiC Nanocomposite Prepared by Atomic Layer Deposition Used as a Novel Electrocatalyst for Nonenzymatic Glucose Sensing," *ACS Appl. Mater. Interfaces,* vol. 7, no. 8, pp. 4772-4777, 2015/03/04 2015, doi: 10.1021/am508508m.

[9] D. Su, M. Ford, and G. Wang, "Mesoporous NiO crystals with dominantly exposed {110} reactive facets for ultrafast lithium storage," *Sci. Rep.,* Article vol. 2, p. 924, 12/05/online 2012, doi: 10.1038/srep00924 https://www.nature.com/articles/srep00924#supplementary-information.

[10] S. Mishra, S. Lambora, P. Yogi, P. R. Sagdeo, and R. Kumar, "Organic Nanostructures on Inorganic Ones: An Efficient Electrochromic Display by Design," *ACS Appl. Nano Mater.,* vol. 1, no. 7, pp. 3715-3723, 2018/07/27 2018, doi: 10.1021/acsanm.8b00871.

[11] J. Melskens, B. W. H. Loo, B. Macco, L. E. Black, S. Smit, and W. M. M. Kessels, "Passivating Contacts for Crystalline Silicon Solar Cells: From Concepts and Materials to Prospects," *IEEE J. Photovolt.,* vol. 8, no. 2, pp. 373-388, 2018, doi: 10.1109/JPHOTOV.2018.2797106.

[12] M. T. Greiner, M. G. Helander, W.-M. Tang, Z.-B. Wang, J. Qiu, and Z.-H. Lu, "Universal energy-level alignment of molecules on metal oxides," *Nat. Mater.,* Article vol. 11, p. 76, 11/06/online 2011, doi: 10.1038/nmat3159 https://www.nature.com/articles/nmat3159#supplementary-information.

[13] M. Nachman, L. N. Cojocaru, and L. V. Rîbco, "Electrical Properties of Non-Stoichiometric Nickel Oxide," *Phys. Status Solidi,* vol. 8, no. 3, pp. 773-783, 1965, doi: doi:10.1002/pssb.19650080316.

[14] I. Bransky and N. M. Tallan, "High-Temperature Defect Structure and Electrical Properties of NiO," *J. Chem. Phys.,* vol. 49, no. 3, pp. 1243-1249, 1968, doi: 10.1063/1.1670215.

[15] C. C. Boyd *et al.*, "Overcoming Redox Reactions at Perovskite-Nickel Oxide Interfaces to Boost Voltages in Perovskite Solar Cells," *Joule,* vol. 4, no. 8, pp. 1759-1775, 2020/08/19/ 2020, doi: https://doi.org/10.1016/j.joule.2020.06.004.

[16] J. Y. Zhang *et al.*, "Electronic and transport properties of Li-doped NiO epitaxial thin films," *J. Mater. Chem. C,* 10.1039/C7TC05331B vol. 6, no. 9, pp. 2275-2282, 2018, doi: 10.1039/C7TC05331B.

[17] F.-H. Hsu *et al.*, "Enhanced carrier collection in p-Ni1−xO:Li/n-Si heterojunction solar cells using LiF/Al electrodes," *Thin Solid Films,* vol. 573, pp. 159-163, 2014/12/31/ 2014, doi: https://doi.org/10.1016/j.tsf.2014.11.025.

[18] Y. R. Denny *et al.*, "Electronic, electrical and optical properties of undoped and Na-doped NiO thin films," *Thin Solid Films,* vol. 591,

pp. 255-260, 2015/09/30/ 2015, doi: https://doi.org/10.1016/j.tsf.2015.04.043.

[19] N. Wang *et al.*, "Structural, electrical and optical properties of K-doped NiO films prepared by rapid pyrolysis sol-gel technique," *Thin Solid Films,* vol. 616, pp. 587-593, 2016/10/01/ 2016, doi: https://doi.org/10.1016/j.tsf.2016.08.051.

[20] S. Dewan, M. Tomar, R. P. Tandon, and V. Gupta, "Zn doping induced conductivity transformation in NiO films for realization of p-n homo junction diode," *J. Appl. Phys.,* vol. 121, no. 21, p. 215307, 2017, doi: 10.1063/1.4984580.

[21] S. Nandy, U. N. Maiti, C. K. Ghosh, and K. K. Chattopadhyay, "Enhanced p-type conductivity and band gap narrowing in heavily Al doped NiO thin films deposited by RF magnetron sputtering," *J. Phys. Condens. Matter,* vol. 21, no. 11, p. 115804, 2009/02/24 2009, doi: 10.1088/0953-8984/21/11/115804.

[22] T. Zhang, M. A. Hossain, C.-Y. Lee, Y. Zakaria, A. A. Abdallah, and B. Hoex, "Atomic layer deposited ZnxNi1−xO: A thermally stable hole selective contact for silicon solar cells," *Appl. Phys. Lett.,* vol. 113, no. 26, p. 262102, 2018, doi: 10.1063/1.5056223.

[23] C. I. Bright, "Review of Transparent Conductive Oxides (TCO)," *Soc. Vac. Coaters Bulletin,* pp. 38–48, 2007.

[24] G. Kresse and D. Joubert, "From ultrasoft pseudopotentials to the projector augmented-wave method," *Phys. Rev. B,* vol. 59, no. 3, pp. 1758-1775, 01/15/ 1999. [Online]. Available: https://link.aps.org/doi/10.1103/PhysRevB.59.1758.

[25] J. Heyd, G. E. Scuseria, and M. Ernzerhof, "Hybrid functionals based on a screened Coulomb potential," *J. Chem. Phys.,* vol. 118, no. 18, pp. 8207-8215, 2003, doi: 10.1063/1.1564060.

[26] D. S. Lambert, A. Lennon, and P. A. Burr, "Extrinsic Defects in Crystalline MoO3: Solubility and Effect on the Electronic Structure," *J. Phys. Chem. C,* vol. 122, no. 48, pp. 27241-27249, 2018/12/06 2018, doi: 10.1021/acs.jpcc.8b09226.

[27] H. M.A. *et al.*, "Transition Metal Oxides as Passivated Hole-Contacts Layer for Silicon Solar Cells: Intrinsic and Extrinsic Defects in MoO3 from First-Principles Calculations," *35th EU PVSEC 2018,* pp. 15 - 19, 2018, doi: 10.4229/35thEUPVSEC20182018-1AO.1.6.

[28] H. J. Monkhorst and J. D. Pack, "Special points for Brillouin-zone integrations," *Phys. Rev. B,* vol. 13, no. 12, pp. 5188-5192, 06/15/ 1976, doi: 10.1103/PhysRevB.13.5188.

[29] D. A. H. Hanaor, M. H. N. Assadi, S. Li, A. Yu, and C. C. Sorrell, "Ab initio study of phase stability in doped TiO2," *Comput. Mech.,* journal article vol. 50, no. 2, pp. 185-194, August 01 2012, doi: 10.1007/s00466-012-0728-4.

[30] S. L. Dudarev, G. A. Botton, S. Y. Savrasov, C. J. Humphreys, and A. P. Sutton, "Electron-energy-loss spectra and the structural stability of nickel oxide: An LSDA+U study," *Phys. Rev. B,* vol. 57, no. 3, pp. 1505-1509, 01/15/ 1998, doi: 10.1103/PhysRevB.57.1505.

[31] H. Chen and J. H. Harding, "Nature of the hole states in Li-doped NiO," *Phys. Rev. B,* vol. 85, no. 11, p. 115127, 03/28/ 2012, doi: 10.1103/PhysRevB.85.115127.

[32] R. Long, N. J. English, and D. A. Mooney, "Electronic structures of N- and C-doped NiO from first-principles calculations," *Phys. Lett. A,* vol. 374, no. 9, pp. 1184-1187, 2010/02/15/ 2010, doi: https://doi.org/10.1016/j.physleta.2009.12.058.

[33] Y. Li, F. Yang, and Y. Yu, "LSDA+U study on the electronic and anti-ferromagnetic properties of Ni-doped CuO and Cu-doped NiO," *Chinese J. Catal.,* vol. 38, no. 5, pp. 767-773, 2017/05/01/ 2017, doi: https://doi.org/10.1016/S1872-2067(17)62796-7.

[34] S. Park *et al.*, "Interaction and ordering of vacancy defects in NiO," *Phys. Rev. B,* vol. 77, no. 13, p. 134103, 04/07/ 2008, doi: 10.1103/PhysRevB.77.134103.

[35] W. B. Zhang, N. Yu, W. Y. Yu, and B. Y. Tang, "Stability and magnetism of vacancy in NiO: A GGA+U study," *Eur. Phys. J. B,* vol. 64, no. 2, pp. 153-158, 2008/07/01 2008, doi: 10.1140/epjb/e2008-00303-x.

[36] J. E. Petersen, F. Twagirayezu, L. M. Scolfaro, P. D. Borges, and W. J. Geerts, "Electronic and optical properties of antiferromagnetic iron doped NiO – A first principles study," *AIP Adv.,* vol. 7, no. 5, p. 055711, 2017/05/01 2017, doi: 10.1063/1.4975493.

[37] D. S. Lambert, S. T. Murphy, A. Lennon, and P. A. Burr, "Formation of intrinsic and silicon defects in MoO3 under varied oxygen partial pressure and temperature conditions: an ab initio DFT investigation," *RSC Adv.,* 10.1039/C7RA10690D vol. 7, no. 85, pp. 53810-53821, 2017, doi: 10.1039/C7RA10690D.

[38] L.-H. Ye, N. Luo, L.-M. Peng, M. Weinert, and A. J. Freeman, "Dielectric constant of NiO and LDA+U," *Phys. Rev. B,* vol. 87, no. 7, p. 075115, 02/13/ 2013, doi: 10.1103/PhysRevB.87.075115.

[39] S. Lany and A. Zunger, "Assessment of correction methods for the band-gap problem and for finite-size effects in supercell defect calculations: Case studies for ZnO and GaAs," *Phys. Rev. B,* vol. 78, no. 23, p. 235104, 12/04/ 2008, doi: 10.1103/PhysRevB.78.235104.

[40] Y. Kumagai and F. Oba, "Electrostatics-based finite-size corrections for first-principles point defect calculations," *Phys. Rev. B,* vol. 89, no. 19, p. 195205, 05/23/ 2014, doi: 10.1103/PhysRevB.89.195205.

[41] R. A. Robie and B. S. Hemingway, "Thermodynamic properties of minerals and related substances at 298.15 K and 1 bar (10^5 pascals) pressure and at higher temperatures," in "Bulletin," Report 2131, 1995. [Online]. Available: http://pubs.er.usgs.gov/publication/b2131

[42] N. D. M. Hine, K. Frensch, W. M. C. Foulkes, and M. W. Finnis, "Supercell size scaling of density functional theory formation energies of charged defects," *Phys. Rev. B,* vol. 79, no. 2, p. 024112, 01/30/ 2009, doi: 10.1103/PhysRevB.79.024112.

[43] S. T. Murphy and N. D. M. Hine, "Point Defects and Non-stoichiometry in Li2TiO3," *Chem. Mater.,* vol. 26, no. 4, pp. 1629-1638, 2014/02/25 2014, doi: 10.1021/cm4038473.

[44] H. Komatsu and M. Ishigame, "Visualization of antiferromagnetic domain structures on as-grown NiO crystals by optical methods," *J. Mater. Sci.,* journal article vol. 20, no. 11, pp. 4027-4034, November 01 1985, doi: 10.1007/bf00552395.

[45] A. Bouzoubaa, D. Costa, B. Diawara, N. Audiffren, and P. Marcus, "Insight of DFT and atomistic thermodynamics on the adsorption and insertion of halides onto the hydroxylated NiO(111) surface," *Corros. Sci.,* vol. 52, no. 8, pp. 2643-2652, 2010/08/01/ 2010, doi: https://doi.org/10.1016/j.corsci.2010.04.014.

[46] K. Lee, Y. Youn, and S. Han, "Identification of ground-state spin ordering in antiferromagnetic transition metal oxides using the Ising model and a genetic algorithm," *Sci. Technol. Adv. Mat.,* vol. 18, no. 1, pp. 246-252, 2017, doi: 10.1080/14686996.2017.1300046.

[47] A. Rohrbach, J. Hafner, and G. Kresse, "Molecular adsorption on the surface of strongly correlated transition-metal oxides: A case study for CO/NiO(100)," *Phys. Rev. B,* vol. 69, no. 7, p. 075413, 02/25/ 2004, doi: 10.1103/PhysRevB.69.075413.

[48] J. Osorio-Guillén, S. Lany, and A. Zunger, "Nonstoichiometry and hole doping in NiO," *AIP Conf. Proc.,* vol. 1199, no. 1, pp. 128-129, 2010, doi: 10.1063/1.3295330.

[49] A. M. Ferrari, C. Pisani, F. Cinquini, L. Giordano, and G. Pacchioni, "Cationic and anionic vacancies on the NiO(100) surface: DFT+U and hybrid functional density functional theory calculations," *J. Chem. Phys.,* vol. 127, no. 17, p. 174711, 2007, doi: 10.1063/1.2796154.

[50] B. E. F. Fender, A. J. Jacobson, and F. A. Wedgwood, "Covalency Parameters in MnO, α-MnS, and NiO," *J. Chem. Phys.,* vol. 48, no. 3, pp. 990-994, 1968/02/01 1968, doi: 10.1063/1.1668855.

[51] J. Linnera, G. Sansone, L. Maschio, and A. J. Karttunen, "Thermoelectric Properties of p-Type Cu2O, CuO, and NiO from Hybrid Density Functional Theory," *J. Phys. Chem. C,* vol. 122, no. 27, pp. 15180-15189, 2018/07/12 2018, doi: 10.1021/acs.jpcc.8b04281.

[52] K. Singh, J. Nowotny, and V. Thangadurai, "Amphoteric oxide semiconductors for energy conversion devices: a tutorial review," *Chem. Soc. Rev.,* 10.1039/C2CS35393H vol. 42, no. 5, pp. 1961-1972, 2013, doi: 10.1039/C2CS35393H.

[53] I. Rom, W. Jantscher, and W. Sitte, "Conductivity relaxation experiments on Ni1−δO," *Solid State Ionics,* vol. 135, no. 1, pp. 731-736, 2000/11/01/ 2000, doi: https://doi.org/10.1016/S0167-2738(00)00398-2.

[54] W. C. Tripp and N. M. Tallan, "Gravimetric Determination of Defect Concentrations in NiO," *J. Am. Ceram. Soc.,* vol. 53, no. 10, pp. 531-533, 1970/10/01 1970, doi: 10.1111/j.1151-2916.1970.tb15958.x.

[55] S. Mrowec and Z. Grzesik, "Oxidation of nickel and transport properties of nickel oxide," *J. Phys. Chem. Solids,* vol. 65, no. 10, pp. 1651-1657, 2004/10/01/ 2004, doi: https://doi.org/10.1016/j.jpcs.2004.03.011.

[56] C. J. Flynn, S. M. McCullough, L. Li, C. L. Donley, Y. Kanai, and J. F. Cahoon, "Passivation of Nickel Vacancy Defects in Nickel

Oxide Solar Cells by Targeted Atomic Deposition of Boron," *J. Phys. Chem. C,* vol. 120, no. 30, pp. 16568-16576, 2016/08/04 2016, doi: 10.1021/acs.jpcc.6b06593.

[57] C. J. Flynn *et al.*, "Site-Selective Passivation of Defects in NiO Solar Photocathodes by Targeted Atomic Deposition," *ACS Appl. Mater. Interfaces,* vol. 8, no. 7, pp. 4754-4761, 2016/02/24 2016, doi: 10.1021/acsami.6b01090.

[58] M. N. Siddique, A. Ahmed, and P. Tripathi, "Enhanced optical properties of pure and Sr doped NiO nanostructures: A comprehensive study," *Optik,* vol. 185, pp. 599-608, 2019/05/01/ 2019, doi: https://doi.org/10.1016/j.ijleo.2019.03.150.

[59] T. Z. H. Gani and H. J. Kulik, "Where Does the Density Localize? Convergent Behavior for Global Hybrids, Range Separation, and DFT+U," *J. Chem. Theory Comput.,* vol. 12, no. 12, pp. 5931-5945, 2016/12/13 2016, doi: 10.1021/acs.jctc.6b00937.

[60] Jonathan Baker, J. Schneider, and S. F. Bent, "Understanding Growth Characteristics of ALD $NiAl_yO_x$: The Role of Ozone," in *19th Internation Conference on Atomic Layer Deposition*, Bellevue, Washington, USA, 2019. [Online]. Available: https://ald2019.avs.org/wp-content/uploads/2019/07/ALD-ALE-2019-Schedule-Master.pdf. [Online]. Available: https://ald2019.avs.org/wp-content/uploads/2019/07/ALD-ALE-2019-Schedule-Master.pdf

[61] L. D'Amario *et al.*, "Chemical and Physical Reduction of High Valence Ni States in Mesoporous NiO Film for Solar Cell Application," *ACS Appl. Mater. Interfaces,* vol. 9, no. 39, pp. 33470-33477, 2017/10/04 2017, doi: 10.1021/acsami.7b01532.

[62] S. Hietzschold *et al.*, "Functionalized Nickel Oxide Hole Contact Layers: Work Function versus Conductivity," *ACS Appl. Mater. Interfaces,* vol. 9, no. 45, pp. 39821-39829, 2017/11/15 2017, doi: 10.1021/acsami.7b12784.

[63] M. N. Siddique, A. Ahmed, and P. Tripathi, "Electric transport and enhanced dielectric permittivity in pure and Al doped NiO nanostructures," *J. Alloy. Compd.,* vol. 735, pp. 516-529, 2018/02/25/ 2018, doi: https://doi.org/10.1016/j.jallcom.2017.11.114.

[64] C. Feng, Z. Jiang, B. Chen, P. Cheng, Y. Wang, and C. Huang, "Aluminum-doped NiO nanofibers as chemical sensors for selective and sensitive methanol detection," *Anal. Methods,* 10.1039/C8AY02460J vol. 11, no. 5, pp. 575-581, 2019, doi: 10.1039/C8AY02460J.